ADVANCED ENERGY MATERIALS
www.advenergymat.de

Rapid Plasma Exsolution from an A-site Deficient Perovskite Oxide at Room Temperature

Hessan Khalid, Atta ul Haq, Bruno Alessi, Ji Wu, Cristian D. Savaniu, Kalliopi Kousi, Ian S. Metcalfe, Stephen C. Parker, John T. S. Irvine, Paul Maguire, Evangelos I. Papaioannou, and Davide Mariotti**

High-performance nanoparticle platforms can drive catalysis progress to new horizons, delivering environmental and energy targets. Nanoparticle exsolution offers unprecedented opportunities that are limited by current demanding process conditions. Unraveling new exsolution pathways, particularly at low-temperatures, represents an important milestone that will enable improved sustainable synthetic route, more control of catalysis microstructure as well as new application opportunities. Herein it is demonstrated that plasma direct exsolution at room temperature represents just such a step change in the synthesis. Moreover, the factors that most affect the exsolution process are identified. It is shown that the surface defects produced initiate exsolution under a brief ion bombardment of an argon low-pressure and low-temperature plasma. This results in controlled nanoparticles with diameters ≈19–22 nm with very high number densities thus creating a highly active catalytic material for CO oxidation which rivals traditionally created exsolved samples.

1. Introduction

Energy applications benefit from the use of a wide range of nanoparticles (NPs) that can be produced with predetermined chemical compositions and high precision.[1] However, nanoparticle integration in application platforms or devices is a major obstacle to full exploitation. Exsolution of nanoparticles has recently emerged as a very promising new approach to resolve some of these challenges for energy conversion, energy storage and catalysis, capable of producing supported nanoparticles in a single synthesis step.[2–7] Exsolution was first observed on stoichiometric perovskite oxides where nanoparticles could be produced from transition metals present on the B-site of the perovskite oxide. This mechanism was initially referred to as solid-state recrystallization or self-regeneration.[8] Recently, however, the use of defect chemistry to synthesize the host oxides has revived the interest in exsolution because it allows a greater number of active cations, enhanced surface nucleation and nanoparticle growth and an overall faster and better controlled process.[3,9,10] Furthermore, the defect chemistry also allows for a structure that does not change when the reaction conditions change from oxidizing to reducing thus producing extremely controllable and stable catalysts. These advances have triggered fast growing research activities in the exsolution of nanoparticles and their application for environmental catalysis, solid oxide fuel cells, electrolysers, and chemical looping.[11–19] Exsolution is now an established term that refers to the growth of nanoparticles via the supply of metallic ionic species from an oxide host. This allows the formation of well anchored and partially embedded nanoparticles (socketed) on the support oxide, while also exhibiting crystallographic alignment. The application interest in exsolved nanoparticles

H. Khalid, A. u. Haq, B. Alessi, P. Maguire, D. Mariotti
Nanotechnology and Integrated Bio-Engineering Centre (NIBEC)
Ulster University
Newtownabbey BT37 0QB, UK
E-mail: khalid-h@ulster.ac.uk; d.mariotti@ulster.ac.uk

J. Wu, S. C. Parker
Department of Chemistry
University of Bath
Claverton Down Bath BA2 7AX, UK

The ORCID identification number(s) for the author(s) of this article can be found under https://doi.org/10.1002/aenm.202201131.

DOI: 10.1002/aenm.202201131

C. D. Savaniu, J. T. S. Irvine
School of Chemistry
University of St. Andrews
Scotland Fife KY16 9ST, UK

K. Kousi
Department of Chemical and Process Engineering
University of Surrey
Guildford, Surrey GU2 7XH, UK

I. S. Metcalfe, E. I. Papaioannou
School of Engineering
Newcastle University
Newcastle upon Tyne NE1 7RU, UK

originates from very distinctive characteristics of exsolved nanoparticles versus nanoparticles that are deposited or grown onto a surface,[20–23] i.e., via impregnated precursors followed by decomposition and thermal reduction. Exsolved nanoparticles, because of their socketed growth and crystallographic alignment, offer high durability and stability under reaction conditions as well as significant resistance to agglomeration and poisoning.[3,9] Furthermore, evidence of improved activity, efficiency, and versatility have been also reported for exsolved nanoparticles across multiple areas of application.[14,24]

Exsolution is initially determined by surface reduction, which produces oxygen defects and provides a driving force for the transport of metal ions from the bulk of the oxide to the surface. This ultimately leads to the stabilization of surface segregated metal particles.[25,26] Exsolution has been demonstrated by thermal reduction using hydrogen for the most part but also using carbon monoxide and methane.[25] These exsolution processes generally require strongly reducing conditions using relatively dry H_2 at high temperatures (400–900 °C) and extended heating periods of several hours. With a thermal approach, exsolution quality can be simply controlled by the input energy. However, thermal exsolution is time-consuming and energy-demanding. Its use is limited to materials that are able to withstand these high-temperature environments, therefore restricting its exploration to a reduced set of chemical combinations.[3] This is also a potential drawback for many catalytic applications, where a harsh treatment of the catalyst could potentially affect properties, such as surface area. As surface reduction and defects trigger exsolution,[27,28] other reduction methods should be capable of producing exsolved nanoparticles.[29] Plasma have been therefore used to supply reducing radicals, which were delivered to a heated substrate to promote exsolution (>650 °C and 1 h).[29] In this type of plasma-enhanced exsolution, the plasma acted as the source of reducing chemical agents. As nitrogen radical species were used in this particular case, contamination with oxynitride species was also observed on the oxide. When an argon plasma was used (>650 °C and 1 h), exsolution was also observed however such high temperature process remained unexplained.[29] Exsolution has been also shown to occur in a few minutes under a reducing electron beam within a transmission electron microscope.[30] Electron-beam irradiation offers limited technological opportunities but can be important in revealing underlying exsolution mechanisms with temporal resolution. Another interesting approach that allows very fast (a few minutes) exsolution and at low temperature is electrochemical switching.[28] In this case both the electron flux and the oxygen partial pressure gradient are responsible for the exsolution of nanoparticles at high density. This approach is limited however to electrochemical applications where the perovskite can be deposited as an electrode film. The work produced so far highlights clear opportunities to better understand exsolution mechanisms and improve performance for use in a wide range of applications, including catalysis. Achieving low-temperature exsolution while overcoming the limitations of electrochemical poling is an important goal that would open up exsolution to a much wider range of oxide chemistries and promote opportunities for tailoring nanoparticle chemical compositions, thereby attracting interest from well beyond the field of high-temperature electrochemical devices. There is also the interest in steering away from using gaseous reducing chemical agents, hence simplify the exsolution process requirements.

Here we demonstrate direct low-temperature plasma exsolution for the first time. In this process, the plasma does not supply reducing radicals and the traditional high temperature exsolution by chemical reduction is thereby avoided. Instead exsolution is promoted via oxygen defects directly created by physical means. We observe that exsolution in an argon low-pressure low-temperature plasma is initiated on an A-site deficient perovskite oxide as soon as the oxide is exposed to the plasma. Large particle densities with diameters in the range 19–22 nm were achieved at room temperature within 15 min. These results pave the way to new research directions to understand the fundamentals of direct plasma exsolution, exsolution with new materials and chemistries as well as new application avenues that have been limited thus far due to the requirement for high temperature processing.

2. Results

In order to demonstrate low-temperature direct plasma exsolution, we have selected a nonstoichiometric (A-site deficient) perovskite oxide having a composition of $La_{0.43}Ca_{0.37}Ti_{0.94}Ni_{0.06}O_{2.955}$ (LCTN) and an A-site deficiency of 20%. LCTN was selected because it allows us a direct comparison with other exsolution methodologies and previous catalytic studies.[25,28,31–33] We have carried out a full materials characterization that demonstrates the exsolution of nanoparticles and have investigated the process time-dependence. These include scanning and electron microscopy, X-ray photoelectron spectroscopy, X-ray diffraction, and Raman spectroscopy. We confirm that Ni exsolution is taking place and we highlight that other phenomenon may be possible with a greater degree of process control and an intimate understanding of the fundamental mechanisms involved. Finally, we demonstrate the catalytic activity of plasma-exsolved nanoparticles in the CO oxidation reaction.

LCTN samples were exposed to the plasma treatment for 15 min (LCTN-15) and material characterization was carried out to observe plasma exsolution and compare with pristine LCTN samples. The incorporation of A-site deficiencies is expected to trigger the B-site exsolution with good coverage and higher surface distribution of exsolved nanoparticles. Scanning electron microscopy (SEM) images in **Figure 1** show the surface morphology of the LCTN and LCTN-15 samples at two different magnifications. LCTN (Figure 1a,b) shows steps and ledges which corresponds toward low index crystallographic planes and such terraced morphology is generally observed in A-site deficient perovskite oxide system.[33] It is evident that the pristine LCTN sample shows no sign of exsolved nanoparticles on the surface while, after 15 min of plasma treatment (Figure 1c,d), extensive nanoparticle exsolution is observed.

The exsolution in LCTN-15 shows that the nanoparticles are well distributed over different locations of the pellet (see Section-A, Supporting Information). The average nanoparticle size is 19.7 nm, whereas the population density is ≈550 μm^{-2} (**Figure 2**a; and also Section-A of the Supporting Information). The particle diameter is within the same range

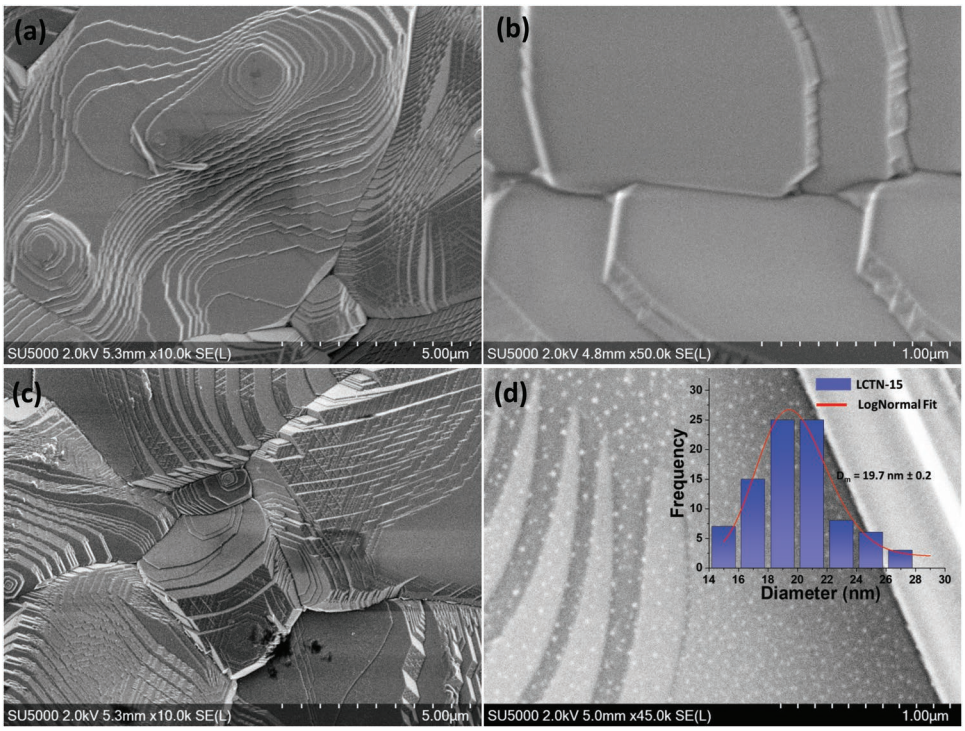

Figure 1. Low and high magnification Field-emission scanning electron microscopy images of a,b) as synthesized LCTN sample and c,d) after argon plasma treatment (15 min). Inset shows the size distribution of the exsolved nanoparticles from LCTN-15.

of previous reports for LCTN exsolution via thermal reduction, but the particle density appears to be distinctly higher than most reports.[28] In thermal exsolution, the size and density of the nanoparticles can vary, depending on experimental conditions. For instance, for LCTN exsolution, particle diameters of 20–41 nm have been mostly reported with population densities of 7–90 μm^{-2} (see also Section L, Supporting Information). Smaller ≈11 nm particles with a density of 80 μm^{-2} have also been reported for LCTN by thermal exsolution.[29] We have also explored plasma exposure for shorter and longer times (see Section-A, Supporting Information) and have summarized the trend of particle average size/density in Figure 2a (see also Section-A, Supporting Information). These have shown calculated average particle diameters of about 21 and 20 nm for 10 min (LCTN-10) and 20 min (LCTN-20) plasma treatment, respectively, while the respective densities were 60 and 510 μm^{-2}.

The average particle size does not change dramatically with time and we consider these differences to be negligible. However, the particle density after 10 min plasma processing is much lower than that after 15 and 20 min plasma exposure. These results show that particles are quickly exsolved with the number of particles that depend on the time of the process and reaching a saturation point after 15 min. Hence, the dynamics of the exsolution is very similar to that observed during electrochemical poling and in situ electron microscopy, i.e., nucleation and growth take place within the very first few minutes and it is overall much faster than that achieved by hydrogen reduction which normally takes 10–30 h.[25,28] The number of Ni atoms exsolved and the distance from the surface that these originated from (exsolution depth), (Figure 2a), can be estimated following simple geometric and crystal structure information (Section-C, Supporting Information), assuming metallic

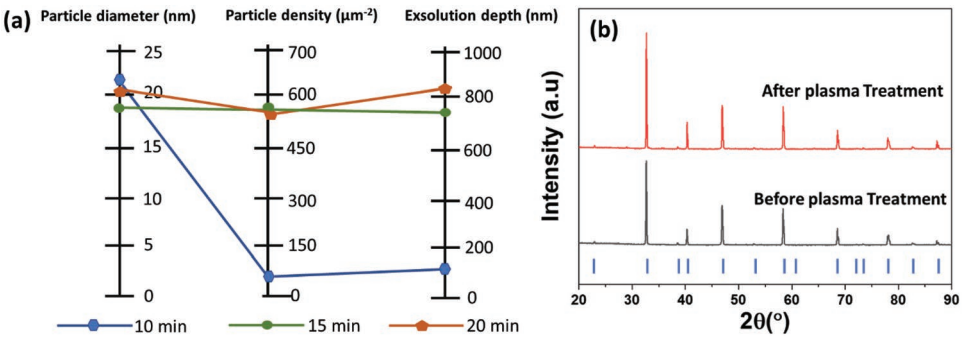

Figure 2. a) Analysis of exsolved nanoparticles characteristics for different plasma exposure time. b) XRD analysis before and after 15 min plasma treatment. Blue vertical bar in (b) depicts the Bragg's position of reference perovskite phase.

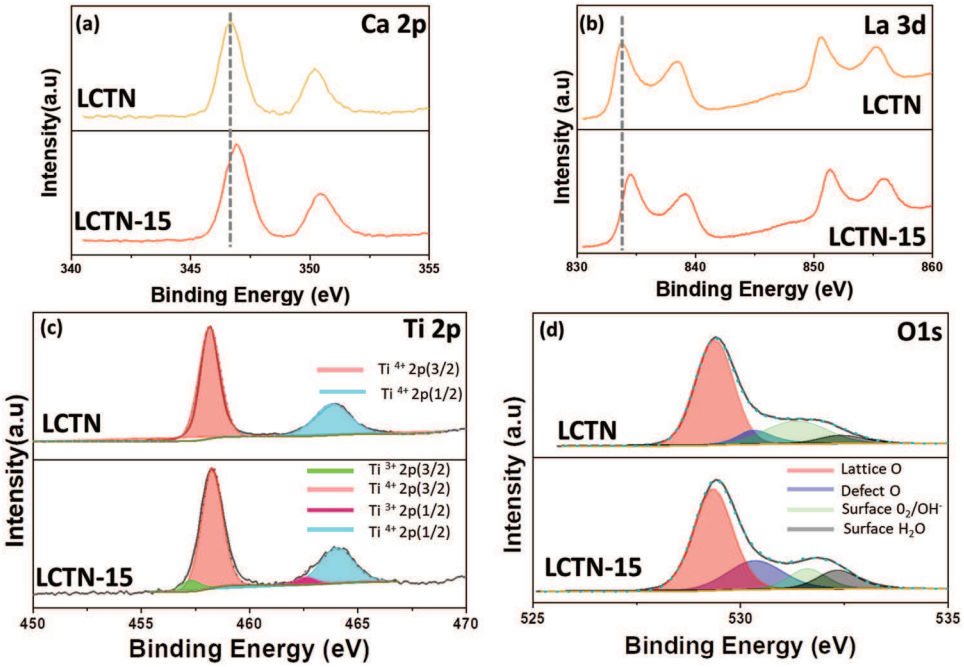

Figure 3. X-ray photoelectron spectroscopy (XPS) results. XPS spectra of a) Ca 2p and b) La 3d indicating shift on A-site ion before and after plasma treatment. High resolution XPS spectra (deconvoluted) of c) Ti 2p and d) O 1s before and after plasma treatment.

Ni nanoparticles.[9,34] The exsolution depth was 110, 752, and 810 nm for 10, 15, and 20 min plasma processing, respectively. The large values of exsolution depth obtained for processing times above 10 min result directly from the corresponding high particle densities (>500 μm^{-2}) at these conditions, compared, e.g., with LCTN H_2 driven thermal exsolution with comparable particle diameters (≈20 nm) where an exsolution depth of ≈80 nm and with particle densities of 90 μm^{-2} were achieved.[28]

The X-ray diffraction (XRD) pattern of the pristine LCTN sample before plasma treatment (Figure 2b) indicates the phase purity of the as-synthesized LCTN pellet, with a single perovskite phase observed without impurities or any precipitated phase. XRD of the sample after 15 min plasma treatment is shown in Figure 2b and present the same pattern as the pristine LCTN, which indicates that the plasma treatment did not introduce major changes to the bulk structure of the perovskite oxide. In our XRD pattern, the peak at ≈44.5° corresponding to Ni (111) was not observed. However, this peak is not expected if particles were sufficiently small, oxidized or low in density with respect to the volume probed by the XRD. The Ni (111) peak has been observed with exsolved nanoparticles when nanoparticles were thermally exsolved with larger diameters than the plasma exsolved nanoparticles reported here. Literature reports for thermally exsolved particles with sizes that are comparable to ours consistently show the absence of the Ni (111) peak (see Section-L, Supporting Information). Our XRD results are also consistent with findings in the literature for exsolution by various other techniques such as thermal shock and electrochemical poling, at similar sizes.[33,35,36]

X-ray photoelectron spectroscopy (XPS) (**Figure 3**) was used to investigate the surface composition as well as the nature of the exsolved nanoparticles. Unfortunately, the main line of La *3d* and Ni *2p* overlap with each other so that the Ni oxidation state cannot be confirmed directly. The Ca *2p* and La *3d* peaks (Figure 3a,b) experience a shift in their binding energy after plasma treatment. In $LaFeO_3$-based perovskite oxide systems, after exsolution, a similar shift has been observed and attributed to stoichiometric changes.[37] The shift has been also attributed to an enrichment of A-site cations where A/B ratio was increased (demonstrated by XPS), gradually filling the A-site vacancies and possibly contributing toward the locking of the exsolved particles exsolution.[9] The initial LCTN chemical composition shows 100% Ti^{4+}, whereas after 15 min plasma treatment a mixed ionic state (≈89% Ti^{4+} and 11% Ti^{3+}) is observed indicating the removal of oxygen from the lattice positions (Figure 3c). As shown in Figure 3d, O *1s* can be fitted into four components. The peaks at binding energy of 529, 530.5, 531.5, and 532.55 eV are attributed to lattice oxygen, oxygen vacancies, surface oxygen species, and surface H_2O, respectively.[38,39] The peak at 530.5 eV (attributed to oxygen vacancies) results in an increase from 11% to 18% after plasma treatment. Similarly, the oxygen peak associated with lattice oxygen shows a decrease from 68% to 56%. This is consistent with the reduction of Ti^{4+} to Ti^{3+} resulting from energetic species, which create oxygen vacancies as indicted by O 1*s*. We have also checked that this is not due to changes in adventitious carbon or due to other oxides (Section-B, Supporting Information). Similarly, the valence band maxima (VBM) of LCTN was positioned at ≈1.9 eV, whereas after plasma treatment, the VBM dropped to 0.9 eV (Section-B, Supporting Information). This shift in VBM has been attributed to the defect creation in surface defective TiO_2 systems.[40]

Transmission electron microscopy (TEM) analysis of the LCTN-15 sample (**Figure 4**) is a good representation of the nature of socketing of the exsolved nanoparticles with the matrix. High resolution TEM images along with their corresponding inverse fast Fourier transforms (FFTs) are shown in

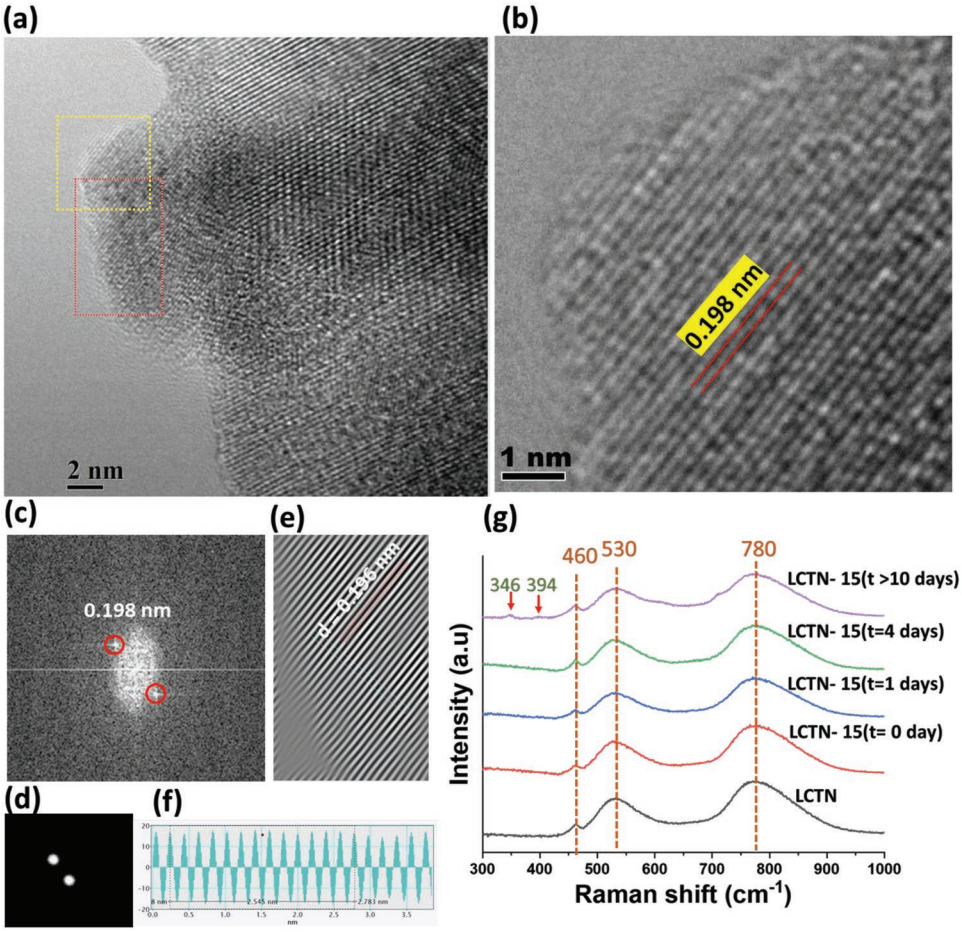

Figure 4. a) HR-TEM image of exsolved NP from LCTN. b) A magnified image of the lattices fringes in the exsolved NP taken from the region highlighted in yellow square box. c) FFT of the selected region (highlighted in red) in (a). d) Masked spots of FFT. e) Inverse FFT of the masked spots resulting in the corresponding lattice fringes. f) Line profiles of inverse FFT resulting in the average lattice spacing value of around 0.196 nm corresponding to plane of Ni. g) Raman Spectra of LCTN before and after plasma treatment (LCTN-15) at different time interval to track the chemical changes within the exsolved nanoparticles.

Figure 4a–e. The d-spacing from FFT (Figure 4c) as well as from the lattice fringes (Figure 4e) show that the exsolved nanoparticles have a lattice spacing of 0.198 and 0.196 nm (Figure 4c–e) which is in agreement with the metallic nickel (111) plane (JCPDS 00-004-0850). In the Supporting Information, we have included further TEM images and corresponding analyses, which shows that the identification on the crystal structure on the particle is occasionally challenging and that oxidized particles are also present (see Section-A, Supporting Information) or may indicate that A-site cation segregation, exsolving in the form of oxide, has taken place.[41]

Raman spectra of the LCTN and LCTN-15 sample can be seen in Figure 4g. The peaks at 780 and 530 cm^{-1} matches closely to similar phonon modes in perovskite systems (ABO_3)[42] and do not exhibit any changes after the plasma treatment. For similar perovskite oxide systems, NiO peaks are usually observed at 344, 394, and 450 cm^{-1},[42] with the latter also present in the pristine LCTN sample (measured at 460 cm^{-1}). After plasma exsolution no extra peaks are observed, however two peaks at 346 and 394 cm^{-1} appear after several days of exposure in air.

The analysis demonstrates rapid and direct plasma exsolution at low-temperature after low-pressure plasma treatment. The results suggest that Ni atoms are being exsolved and the formation of Ni nanoparticles is observed, in agreement with the same or similar oxide systems.[28,43] Oxidation of the Ni particles is also likely either at the surface during exsolution or when exposed to the atmosphere after exsolution.

2.1. Discussion on Exsolution Mechanisms

A surface exposed to a plasma is bombarded by positive ions and electrons and develops a surface electron charge layer along with an electrical potential difference with respect to the center of the plasma. This is due to the much higher electron mobility compared to ions upon initial exposure of the surface leading to much higher electron flux to the surface. A "plasma sheath" region, supporting an electric field, is then formed close to the surface. After the potential difference and sheath are established, the system reaches a steady-state where positive and negative charge fluxes to the surface are equal

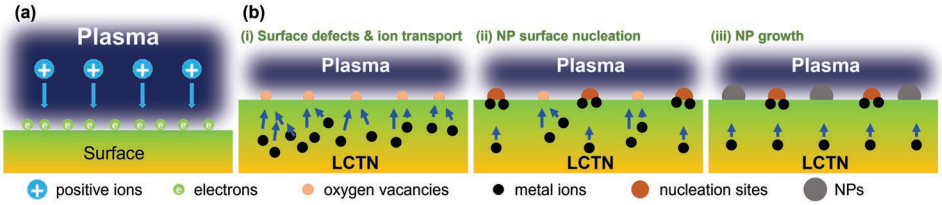

Figure 5. a) Ion bombardment on the LCTN surface due to the presence of plasma sheath near the surface. b) Schematic representation of plasma driven exsolution of Ni nanoparticles indicating various phenomena occurring during the process.

(**Figure 5**a, see also Section-D3 of the Supporting Information).[44] However, locally and in the short-time period (ns), the surface charge may vary from the overall average value. During the plasma process, positively charged ions are accelerated through the plasma sheath. The potential difference is generally affected by the reactor geometry and the substrate may experience a self-bias which enhances that potential difference between the plasma bulk and the surface in contact with the plasma.

We estimate that the ions from the plasma can impinge on the sample surface with energies in the range of 10–40 eV (Section-D2-3, Supporting Information) introducing surface oxygen defects and causing sputtering of atoms, affecting a depth up to ≈2 nm. The energy required to create a surface oxygen vacancy was calculated using DFT based on a $3 \times 3 \times 4$ pseudocubic $CaTiO_3$ model, where the bottom two $CaTiO_3$ layers were fixed to represent the bulk behavior. The DFT calculations showed that adding one oxygen vacancy on CaO (001) surface of this model lattice required 4.84 eV, while adding one oxygen vacancy on the same surface but with Ni doping required 5.38 eV. These energies are quite high and not achievable by conventional high temperature reduction, hence oxygen vacancy creation will be negligible. In the plasma treatment case, both oxygen vacancy formation energies are well within the energy range of ions arriving from the plasma. Hence, when ions interact with the surface of samples, such as LCTN, the surface oxidation state can be reduced by physical defect and oxygen vacancies formation. This process is routinely observed for different metal oxide systems[45–47] and confirmed by our XPS results (Figure 3). We should note that whether or not the creation of oxygen vacancies leaves behind negative charges at the surface, the plasma potential will immediately re-establish the surface charge through the potential difference. In other words, the surface charge density is constant and determined by the plasma state and not by the events at the surface. The surface electron density for a plasma at these conditions can be estimated to be up to 10^{13} m^{-2} (see Section-D4, Supporting Information), which is known to affect surface-supported elementary processes, such as electron-ion recombination. The surface charge also produces an electric field penetrating within the bulk of the oxide that can be estimated to be up to 6×10^{-7} V $Å^{-1}$ (see Section-D4, Supporting Information).

Having confirmed direct plasma exsolution experimentally, we can provide a qualitative description of the potential mechanisms involved in the plasma exsolution of nanoparticles (Figure 5b): i) Ni ion transport from below the surface due to surface defects, ii) nucleation at the surface, and iii) nanoparticle growth due to continuous Ni ion supply.

(i) Ni ion transport from below the surface due to surface defects

The generation of surface oxygen vacancies can create local diffusion conditions for Ni ions to transport from the subsurface toward the surface. In order to assess the extent of the reduction in energy for a Ni atom nearing the surface and/or oxygen vacancies, we have calculated the difference in

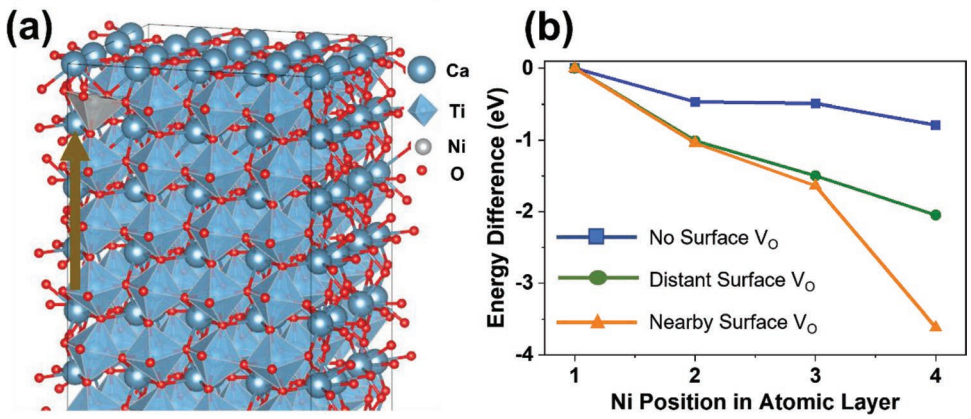

Figure 6. a) Illustration of the surface $CaTiO_3$ slab model used for pair-potential simulation and the positions of the Ni atoms. b) Energy change with respect to Ni position and availability of a nearby surface oxygen vacancy (V_O). "No surface V_O" refers to the case where no surface vacancy is included. "Nearby surface V_O" is designed as an oxygen vacancy right above the segregated Ni, while the "Distant surface V_O" case is designed as an oxygen vacancy at the 3rd nearest neighbor site to the segregated Ni. The atomic layer is counted from the deepest atomic layer (deepest layer = 1; top-most layer = 4). The case containing deepest Ni position is taken as the reference energy state.

segregation energy.[43] Our pair potential based simulations revealed that a reduction in energy is observed for Ni atoms close to the surface (**Figure 6**b, "No surface V_O"), which agrees with earlier report by Gao et al.[48] Furthermore, the segregation energy is further reduced, providing a much stronger stabilization, when oxygen vacancies are introduced (Figure 6b, "Distant/Nearby surface V_O"). The presence of even a single surface oxygen vacancy can significantly lower the Ni segregation energies by more than 3 eV as shown in Figure 6b. Such a significant stabilization effect generates a chemical potential gradient sufficient to change the nearby energetic landscape, lowering the A-site and B-site vacancy formation energies and increasing the diffusion of Ni atoms, allowing for the segregation of Ni dopants at lower temperature as the experiments demonstrate. Given these results for only one oxygen vacancy, we can only expect that the large amount of surface oxygen vacancies created by the plasma treatment will have extensive repercussions on the chemical potential gradient, which will act as a very strong driving force to create mobile species (A-site and B-site cation vacancies) and accelerate the transport. This can explain our experimental observations of the transport and subsequent exsolution at low temperatures during surface plasma treatment.

The electric field produced by the surface charge and within the bulk of the material could in principle promote ion transport, however our calculations (see Section-F, Supporting Information) show that the electric field strength required to have an impact on the Ni ion transport is larger than the breakdown field strength of the host compound (e.g., $\approx 2 \times 10^8$ V m^{-1} for strontium titanate).[49] Therefore, the exsolution depth is determined and limited by the reach of the segregation driving force enhancement induced by surface defect structures and where the creation of oxygen vacancies is an essential enabling step.

(ii) Nucleation at the surface

As the segregation driving force is enhanced toward the defect sites, this provides the opportunity for nucleation of incoming metal ions from the oxide, which are subsequently neutralized by the net negative surface charge established through the plasma sheath. Also, the Ni ions reaching the surface will move due to adatom surface diffusion and have a much higher chance of reaching an oxygen deficiency or defect than being neutralized (Section-G, Supporting Information). While the electric field is not sufficient to draw Ni ions to the surface, the neutralization step due to the negative surface charge prevents the build-up of a positive Ni ion charge and associated electric field which would then oppose further Ni ion migration. The surface charge density therefore appears to be a key feature to enable rapid exsolution, which is also a characteristic feature in the rapid exsolution by electrochemical poling and by in situ electron microscopy. However, because the generation of oxygen vacancies and defects are only a surface phenomenon (< 2 nm), nanoparticle nucleation occurs only at the surface and no (endo)particles are expected within the bulk. The sites where oxygen vacancies/defects are formed therefore correspond to the nucleation sites for nanoparticles and because ion bombardment is more effective and efficient in creating oxygen vacancies and defects than hydrogen reduction, the plasma produces more nucleation sites that translate into a high particle surface density as shown in Figure 2a. From the time evolution of the exsolution process, we can observe that new nucleation sites are formed up to 15 min of plasma exposure. Considering that defect formation from ion bombardment is a much faster process than ion transport, the results suggest that the nucleation is supply limited, i.e., determined by the ion transport kinetics.

(iii) Nanoparticle growth and Ni ion continued supply

Ni ions that contribute to nanoparticle growth are still attracted to the surface due to deformation energies from either the oxide boundaries with the Ni nuclei or surface defects that have not formed nucleation sites yet. In Volmer–Weber growth theory,[50] adatom–adatom interactions are stronger than adatom-surface interactions leading to the nanoparticle growth at the existing nucleation sites. Furthermore, the surface charge and the presence of metallic nanoparticles can form electric field patterns parallel to the surface that can decrease in a meaningful way the surface diffusion activation energy and increase the corresponding diffusion constant.[51–53] Ni ions reaching the growing nanoparticles will be neutralized by the negative charge accumulated by the nanoparticles. This charge is constantly replenished from the plasma as it depends only on the electron temperature and the ion-electron mass ratio.[54]

The growth process is observed from the start of the plasma process, but tends to saturate for exposures longer than 15 min. Therefore, for the most part, nucleation and growth occur simultaneously and both appear to be limited by the supply of Ni ions, which prevents nanoparticle formation and growth after 15 min of plasma exposure. We should also note that for processing times > 15 min, the particle size distribution (Section B-Supporting Information) and density (Figure 2a), hints at a reorganization of the nanoparticles and/or damage of the surface by ion bombardment. With regard to oxidation, this may have occurred once the samples are taken out from the plasma setup and are exposed to the environment as our Raman analysis suggests (Figure 4g). However, we should note that ion bombardment creates oxygen radicals at the surface and oxidation can take place at the surface during exsolution (Section-A, Supporting Information). The energy supplied by the ion flux at the surface could also promote higher surface mobility and therefore overall enhance the oxidation reactions of the growing Ni nuclei and nanoparticles.

The formation of oxygen vacancies and defects by ion bombardment and the establishment of a surface electron density are the key factors that differentiate our direct plasma exsolution from thermal exsolution. As these two key plasma-specific mechanisms do not require thermal energy to be supplied, they allow for low-temperature exsolution to take place. Plasma exsolution has some similarities with several other exsolution methods that have recently been reported,[25,28,29,35] however a detailed comparison is at this stage premature as many of these new techniques are still being investigated. We can note that the choice of plasma system and configuration has an impact on the exsolution outcomes. For instance, the use of a plasma in a remote configuration[29] reduces the ion flux and ion energy which may adversely impact on the plasma ability to produce oxygen vacancies, thus restricting exsolution at low temperature.

2.2. CO Oxidation Tests

To investigate the catalytic activity of the plasma exsolved nanoparticles and confirm that the application performance is not compromised when a low-temperature plasma exsolution process is compared to high-temperature analogues reported in the literature, we employed dense pellets of the LCTN-10, LCTN-15, and LCTN-20 samples and used them as a model catalyst system to link particle characteristics (such as size and population) with catalytic activity in the CO oxidation reaction. Furthermore, the proven coking tolerance of Ni-based exsolved systems is explored for the LCTN-15 sample under CO-rich regions of the CO oxidation reaction and the long-term stability of this sample is tested for up to 100 h. **Figure 7**a shows the CO_2 production rate as a function of temperature (left *y*-axis, which is often referred as light-off experiment) and the corresponding nTOF values as a function of temperature (right *y*-axis). The rate on the left *y*-axis is normalized with respect to the area of the pellet surface decorated with particles.

The minimum temperature for any measurable CO_2 reaction rate was around 300 °C for the LCTN-10 and LCTN-15 samples and around 250 °C for the LCTN-20 sample. Below these temperatures the rate of CO_2 production was below the minimum measurable limit (1×10^{-4} mol s^{-1}). For all three catalysts, the activity increased upon increasing temperature. Across the entire examined temperature range the CO oxidation rates are similar for LCTN-10 and LCTN-20 catalysts, while above 400 °C, the LCTN-15 catalyst showed slightly higher CO_2 production rates. However, it should be noted, that the LCTN-10 catalyst exhibits one order of magnitude less particle population as opposed to the other two catalysts. In order to better compare the site activities between the three catalyst and to the literature data for thermally exsolved Ni particle catalyst systems, we calculate their respective nTOFs for the CO oxidation reaction. For this, we assume that each surface metal atom acts as one active site and the nanoparticles have hemispherical shape as particle analysis data obtained from SEM image analysis indicates in Figure 2a. For all three catalysts the corresponding nTOF values are plotted against temperature on the right *y*-axis in Figure 7a. Consistent with previous reports on thermally exsolved Ni nanoparticles, the nTOF values for the LCTN-15 and LCTN-20 plasma exsolved catalysts are of the order of 10^1–10^2 s^{-1}, i.e., the activity is in the same order of magnitude as that obtained from thermally exsolved nanoparticles.[14,55] Under the same reaction conditions, the nTOF values for the LCTN-10 catalyst are up to one order of magnitude higher (≈800 s^{-1} at 510 °C) than those of the LCTN-15 and LCTN-20 catalysts and a few orders of magnitude higher than values reported in literature for base metal oxide nanoparticles deposited using common deposition techniques, such as chemical impregnation.[56] This difference largely originates from the fact that the particle population of the LCTN-10 catalyst is one order of magnitude lower than that of the other two catalyst samples tested. Also, the LCTN-15 catalyst has slightly smaller nanoparticles as opposed to the LCTN-10 and LCTN-20 catalysts and these appear to be more active at temperature above 400 °C under similar reaction conditions to thermally exsolved Ni nanoparticles.[14] These results indicate that the activity of plasma exsolved nanoparticles can match the activity of the thermally exsolved analogues for CO oxidation.

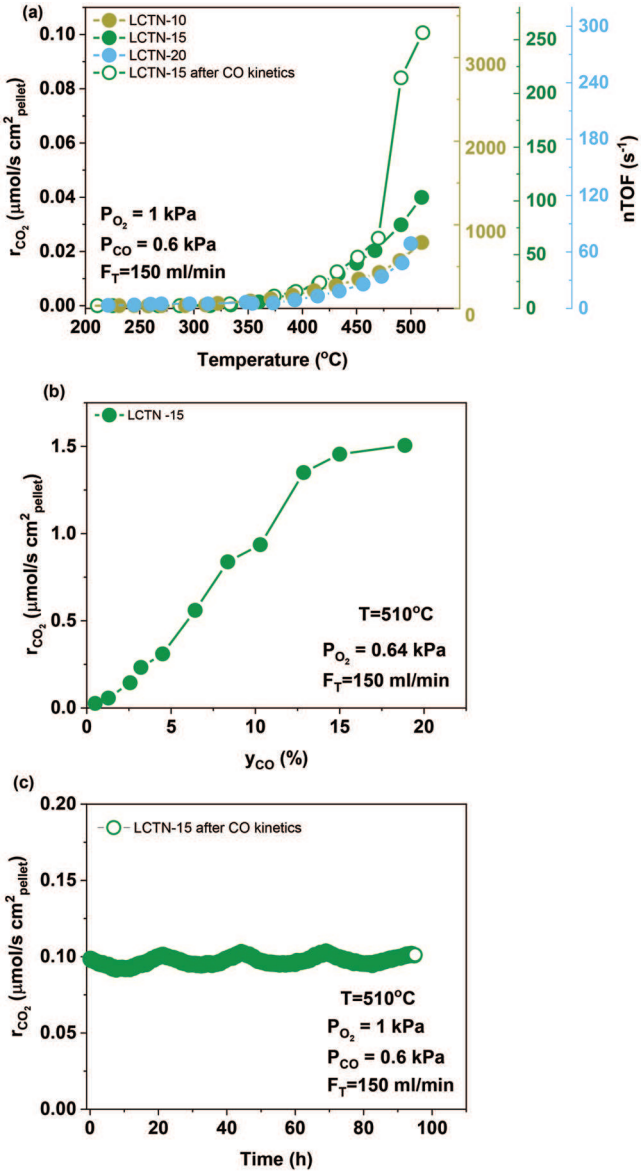

Figure 7. Catalytic activity of plasma exsolved Ni nanoparticles using model (pellet) catalysts. The CO_2 production rate on the left *y*-axis is normalized with respect to the area of the pellet surface decorated with particles. a) CO_2 production rate from the CO oxidation reaction as a function of temperature, b) CO_2 production as a function of mole fraction of CO at 510 °C for the LCNT-15 catalyst. c) CO_2 production rate as a function of time up to 95 h at 510 °C.

Figure 7b shows the CO_2 production rate as a function of the CO mole fraction (y_{CO}) for the LCTN-15 catalyst which showed the highest activity in terms of production rate, r_{CO_2} at 510 °C. Upon increasing the CO mole fraction, the now oxidized LCTN-15 catalyst showed monotonically increasing catalytic rate. No carbon formation was detected by SEM (not shown here) after this experiment, as is the case with thermally exsolved Ni nanoparticles but contrary to base metal oxide nanoparticles prepared by conventional deposition

methods, which in general coke under such high CO mole fractions.[9,57] To investigate the stability of the LCTN-15 catalyst following exposure to high CO mole fractions, we evaluated the catalytic activity in light-off experiment. Interestingly, the CO_2 production rate increased nearly threefold as compared to the first light-off experiment for this catalyst (Figure 7a, denoted as "after CO kinetics"). Not surprisingly, the nTOFs are even higher, of the order of hundreds per second.

We measured the catalytic activity over a period of 95 h of continuous operation at 510 °C in conditions where even though are of practical importance in base metal catalysis, base metal nanoparticles produced by conventional methods typically agglomerate and therefore deactivate in a few hours (Figure 7c).[55] At this point, it should be noted that in the long-term stability test we employed the same pellet sample that was used for the light-off experiment as well as the CO mole fraction dependence experiment, showcasing that the sample was very stable even when subjected to different testing conditions and pretreatments (see also Section-I, Supporting Information). The LCTN-15 catalyst is able to operate at high temperature even after 95 h of continuous testing, similarly with the LCTN sample with thermally exsolved Ni nanoparticles.[14,55] Furthermore, the high catalytic activity, in terms of CO_2 production rate, that was measured after the CO dependence test at 510 °C was maintained throughout the long-term operation. The above results indicate that by using our proposed plasma activated exsolution we can achieve in 10 min and at room temperature highly active catalytic materials something that was up to now only possible through 10 h pretreatments at very high temperatures (≈900 °C).

3. Conclusion

We have demonstrated that an argon low-pressure and low-temperature plasma treatment can promote high density of exsolved nanoparticles from a perovskite oxide in less than 15 min at room temperature. Instead of the much slower chemical reduction mechanism observed in high temperature processes, the plasma exsolution mechanism was shown to be due to activated surface oxygen vacancies and defects, created by physical ion bombardment, which promoted Ni^{2+} migration to surface. The mechanisms of exsolution are based on activation by surface oxygen vacancies/defects that are not produced via chemical reduction but through physical means, i.e., ion bombardment. The plasma-induced negatively-charged surface layer is thought to neutralize metal ions reaching the surface and facilitates to the nanoparticle growth. Plasma exsolution offers the opportunity to produce socketed nanoparticles with crystallographic alignment at low-temperature while avoiding the use of reducing chemical agents. The produced nanoparticles are also as catalytically active as their thermally produced counterparts. Our results therefore represent an important advance and milestone in understanding and broadening nanoparticle exsolution and opens up new research directions for a much wider range of materials with application in catalysis and other energy applications.

4. Experimental Section

Synthesis: Perovskite oxide powder having a composition of $La_{0.43}Ca_{0.37}Ti_{0.94}Ni_{0.06}O_{2.955}$, hereafter LCTN, was synthesized by a citrate sol–gel process. $La(NO_3)_3.6H_2O$ (Alfa Aesar), $Ca(NO_3)_2.4H_2O$, $Ti(C_3H_8NO_3)_2(OH)_2$, and $Ni(NO_3)_2.6H_2O$ (all Sigma-Aldrich), taken in appropriate stoichiometric ratios, were dissolved in deionized water with continuous magnetic stirring at 80 °C. Citric acid ($C_6H_8O_7$, CA) was then added into the solution in the molar ratio CA: total metal atoms 2:1. The solution was evaporated at 150 °C on the hotplate, and the fine powder obtained after combustion was calcined at 850 °C to obtain the LCTN phase. The calcined powder was then pressed into 13 mm diameter pellet using hydraulic press and fired at 1350 °C for 3 h to form dense LCTN pellets.

Exsolution by Plasma: To exsolve particles, the LCTN samples were subsequently plasma treated in an argon low-pressure plasma (Diener Atto 13.56 MHz RF source, see also Section-A of the Supporting Information). Different treatment time (10, 15, and 20 min) and an operating power of 40 W was used to study the phenomenon in detail. Vacuum pressure and input gas pressure were set at 0.3 and 0.4 mbar, respectively. The samples before plasma treatment are denoted as LCTN whereas after 10, 15, and 20 min of argon plasma treatment, these are denoted with LCTN-10, LCTN-15, and LCTN-20, respectively. Samples were placed in the vacuum chamber on a glass holder where only the top surface was directly exposed to the plasma and received post-plasma characterization. During plasma treatment, the sample was not heated and therefore the bulk temperature of the sample is close to room temperature throughout the process (Section-H, Supporting Information).

Material Characterization: Samples were analyzed without further preparation unless explicitly stated. XRD was carried out with a Malvern Panalytical Empyrean-3 to determine the macroscopic crystal structure. XRD was operated in reflection mode at a voltage of 45 kV and current of 40 mA, with Cu Kα radiation (λ = 1.54 Å). The morphology of the top surface of the pellet was initially analyzed by scanning electron microscopy (Fe-SEM Hitachi SU5000), which was used to determine nanoparticle size distribution and mean diameter. Images were acquired at a voltage of 2 kV with a magnification ranging from x10k to x50k. Three images were considered per exsolution condition, and these were analyzed using Image-J software to determine size distribution and population density. The images were converted into binary images in Image-J and the particles were outlined based on the contrast of the nanoparticles from the matrix LCTN. Calculations for particle size distribution, average particle size and number density were carried out assuming the particles have hemi-spherical geometry. XPS was carried out with a ThermoFisher ESCALAB XI instrument. The excitation source used was a monochromated Al operated at 15 kV and 15 mA with a power of 225 W. Charge compensation was employed using a flood gun. Pass energy of 10 eV was used with a dwell time of 50 ms. The recorded spectra of C 1s (reference at 284.8 eV), O 1s, Ti 2p, La 3d, Ca 2p, Ni 3p, and valence band spectrum were sequentially acquired. XPS analysis was done on three different locations on the same sample to validate the results. The data were analyzed using Avantage software. Raman spectroscopy was carried out using an excitation wavelength of 532 nm with Renishaw Invia Qontor system. Raman spectra were collected with a 50x objective lens with a nominal power of 1 mW. The morphology and structure of the exsolved nanoparticles were examined by TEM using JOEL JEM-2100F electron microscope. The surface of the pellet was slightly scratched using a spatula and then few drops of ethanol were put onto the scratched area. With the help of pipette, the ethanol was collected back from the scratched region and then drop-casted directly onto holey carbon mesh/Cu TEM grids which were then dried in air. The high-resolution TEM images and selected area diffraction (SAED) patterns was acquired using the JEOL-JEM-2100F electron microscope operating at 200 kV. The analysis of the lattice fringes of perovskites oxides matrix and the exsolved nanoparticles were carried out using Gatan Microscopy suite Digital Micrograph. The SAED patterns were also analyzed using Digital Micrograph. Standard crystallographic JCPDS cards were used for matching.

Catalytic Characterization: A continuous flow single chamber was used for catalytic activity testing, carried out at atmospheric pressure. A k-type thermocouple was placed in the proximity of the pellet catalyst samples and was used to measure the temperature during the experiment. A fixed-bed reactor filled by Al_2O_3 powder was placed upstream to the single chamber reactor and was used to capture possible carbonyl species from the CO-containing gas cylinder. The 20% CO/He, 20% O_2/He, and CP grade He gases were used, provided by BOC. A flow rate of 1×10^{-4} mol s^{-1} was used throughout the experiments. Helium was used as a balancing gas. In order to study the effect of temperature, the LCTN samples were heated in an inlet gas mixture with 1% of O_2 and 0.6% of CO from 200 up to 510 °C. The temperature was held during the heating of the sample after each step of 20 °C. The holding time varied based on the time the reaction rate becomes steady meaning the rate of CO_2 production does not change by more than ±5% over 1 h. To study CO influence, the O_2 inlet mole fraction was held constant at 0.64%, while the CO mole fraction inlet changed from 0.5% to 18.9%. In order to study the long-term performance, the CO_2 production rate was measured over 90 h under gradientless condition with the reactor operated under differential conversion conditions (i.e., CO conversions below 20%). The CO_2 mole fraction in the product stream was analyzed with an XTREAM-CO_2 analyzer from Rosemount. The minimum measurable CO_2 mole fraction was 1 ppm which corresponds to a minimum measurable CO_2 production rate of 1×10^{-4} mol s^{-1}, which correspond to a volumetric flow rate of 150 cm^3 min^{-1}, at normal temperature and pressure (NTP). The flow rates were also measured at the outlet using a Varian digital flow meter (1000 series). Reaction rates (r_{CO_2}) in terms of CO_2 production are calculated as shown in Equation (1)

$$r_{CO_2}\left(\text{mol}(CO_2)\,s^{-1}m^{-2}\right) = y_{CO_2} \cdot \dot{n} \cdot A^{-1} \quad (1)$$

where (y_{CO_2}) is the measured CO_2 mole fraction at the gas outlet (measured by the XTREAM-CO_2 analyzer), $\dot{n}$ is the molar flow, and A is the top side pellet area where exsolution occurred.

Nominal turnover frequency (nTOF) is calculated as the number of molecules reacted per second, per exposed metal atom site at the surface of particles. To calculate nominal turnover frequency (number of molecules reacted per second, per exposed metal atom site as the surface of the particles, nTOFs) for the catalyst systems Equation (2) is used

$$\text{nTOF}\left(s^{-1}\right) = 10^{-20} \cdot N_A \cdot r_{CO_2} \cdot a^2 / \left(A_e \cdot A_p \cdot k\right) \quad (2)$$

where

r_{CO_2}: is the reaction rate (mol s^{-1})

N_A : is the Avogadro's number (mol^{-1})

A_e: is the surface area of the pellet decorated with particles per total pellet surface area (μm^2 μm^{-2})

A_p : is the exposed particle area per total surface area (cm^2)

a : is the unit cell parameter of the crystal lattice of the particles

k : is the average number of metal sites per unit cell face (the faces were considered to be in a (100) termination, thus, for the NiO rock-salt structure $k = 1$)

Note that the product $(A_e \cdot A)/a^2 \cdot k$ gives the corresponding number of active sites.

Computational Details: To investigate how the plasma treatment affects the exsolution process of Ni dopants in perovskites, a number of density functional theory (DFT) based and Buckingham pair potential based simulations have been carried out. The DFT simulations were completed at the Perdew–Burke–Ernzerhof generalized gradient approximation (GGA-PBE) level with the Vienna ab initio Simulation Package (VASP).[58–61] To address the strong correlation effect of Ni *d* electrons, the energies of the relaxed models were further refined with the hybrid PBE0 functional. The energy cut-offs used for the projector augmented-wave (PAW) pseudopotential based basis sets, as supplied in the VASP package, were 600 eV.[62,63] In all DFT simulations, the electronic cycle convergence criteria were set to 10^{-6} eV, while the ionic cycle convergence criteria were set to –0.03 eV $Å^{-1}$ for the transition state calculations and –0.01 eV $Å^{-1}$ for other calculations. A Monkhorst-Pack k-point mesh of $3 \times 3 \times 1$ was used for the slab models to reflect its anisotropic symmetry. Several defective slab models of perovskite $SrTiO_3$ and $CaTiO_3$ were constructed based on a $3 \times 3 \times 4$ supercell of prerelaxed $SrTiO_3$ and $CaTiO_3$ unit cells. The detailed defect arrangements of these models were included in the Supporting Information. The Buckingham pair potential based simulations were carried out as implemented in the GULP package.[64] The pair potentials used are the Teter Buckingham pair potential, which were derived specifically for solid state ionic materials.[65] These simulations were designed to investigate the impact of additional surface oxygen vacancies on the thermodynamic driving force behind the exsolution. The detailed simulation design and pair potentials parameters are included in the Supporting Information.

Supporting Information

Supporting Information is available from the Wiley Online Library or from the author.

Acknowledgements

The research was supported by EPSRC (Award Nos. EP/R023522/1, EP/R023603/1, EP/R023921/1, EP/R023638/1, EP/R008841/1, and EP/V055232/1) and financial support from the UK Catalysis Hub funded by EPSRC Grant reference EP/R027129/1. J.W. and S.C.P. gratefully acknowledge support from the EPSRC (EP/P007821/1) and also thank the U.K. ARCHER HPC facility and the THOMAS HPC (the UK Materials and Molecular Modelling Hub, partially funded by EPSRC EP/P020194) for providing computation resources, via the membership of the UK's HEC Materials Chemistry Consortium (funded by the EPSRC Grant Nos. EP/L000202, EP/709 P007821/1, EP/R029431, and EP/T022213). This research has also made use of the Balena High Performance Computing (HPC) Service at the University of Bath.

Conflict of Interest

The authors declare no conflict of interest.

Data Availability Statement

The data that support the findings of this study are available in the supplementary material of this article.

Keywords

exsolution, perovskite oxide

Received: April 1, 2022
Revised: September 9, 2022
Published online: October 3, 2022

[1] C. Sun, J. A. Alonso, J. Bian, *Adv. Energy Mater.* **2021**, *11*, 2000459.
[2] J. Zhang, M.-R. Gao, J.-L. Luo, *Chem. Mater. 32*, 5424 **2020**.
[3] D. Neagu, G. Tsekouras, D. N. Miller, H. Ménard, J. T. S. Irvine, *Nat. Chem.* **2013**, *5*, 916.
[4] O. Kwon, S. Joo, S. Choi, S. Sengodan, G. Kim, *J. Phys.: Energy* **2020**, *2*, 032001.
[5] B. A. Rosen, *Electrochem* **2020**, *1*, 32.

[6] K. Kim, C. Lim, J. W. Han, *Korean J. Chem. Eng.* **2020**, *37*, 1295.
[7] K. Kousi, C. Tang, I. S. Metcalfe, D. Neagu, *Small* **2021**, *17*, 2006479.
[8] K. Takehira, *Catal. Surv. Asia* **2002**, *6*, 19.
[9] D. Neagu, T.-S. Oh, D. N. Miller, H. Ménard, S. M. Bukhari, S. R. Gamble, R. J. Gorte, J. M. Vohs, J. T. S. Irvine, *Nat. Commun.* **2015**, *6*, 8120.
[10] G. Tsekouras, D. Neagu, J. T. S. Irvine, *Energy Environ. Sci.* **2012**, *6*, 256.
[11] L. Ye, M. Zhang, P. Huang, G. Guo, M. Hong, C. Li, J. T. S. Irvine, K. Xie, *Nat. Commun.* **2017**, *8*, 14785.
[12] K. Kousi, D. Neagu, L. Bekris, E. I. Papaioannou, I. S. Metcalfe, *Angew. Chem., Int. Ed.* **2020**, *59*, 2510.
[13] D. Hosseini, F. Donat, P. M. Abdala, S. M. Kim, A. M. Kierzkowska, C. R. Müller, *ACS Appl. Mater. Interfaces* **2019**, *11*, 18276.
[14] D. Neagu, E. I. Papaioannou, W. K. W. Ramli, D. N. Miller, B. J. Murdoch, H. Ménard, A. Umar, A. J. Barlow, P. J. Cumpson, J. T. S. Irvine, I. S. Metcalfe, *Nat. Commun.* **2017**, *8*, 1855.
[15] T. Zhu, H. Troiani, L. V. Mogni, M. Santaya, M. Han, S. A. Barnett, *J. Power Sources* **2019**, *439*, 227077.
[16] M. Kothari, Y. Jeon, D. N. Miller, A. E. Pascui, J. Kilmartin, D. Wails, S. Ramos, A. Chadwick, J. T. S. Irvine, *Nat. Chem.* **2021**, *13*, 677.
[17] S.-H. Cui, J.-H. Li, X.-W. Zhou, G.-Y. Wang, J.-L. Luo, K. T. Chuang, Y. Bai, L.-J. Qiao, *J. Mater. Chem. A* **2013**, *1*, 9689.
[18] J. G. Lee, J. H. Myung, A. B. Naden, O. S. Jeon, Y. G. Shul, J. T. S. Irvine, *Adv. Energy Mater.* **2020**, *10*, 1903693.
[19] H. Tanaka, M. Uenishi, M. Taniguchi, I. Tan, K. Narita, M. Kimura, K. Kaneko, Y. Nishihata, J.'I. Mizuki, *Catal. Today* **2006**, *117*, 321.
[20] S. P. Jiang, *Int. J. Hydrogen Energy* **2012**, *37*, 449.
[21] J.-S. Kim, N. L. Wieder, A. J. Abraham, M. Cargnello, P. Fornasiero, R. J. Gorte, J. M. Vohs, *J. Electrochem. Soc.* **2011**, *158*, B596.
[22] S. Helveg, C. López-Cartes, J. Sehested, P. L. Hansen, B. S. Clausen, J. R. Rostrup-Nielsen, F. Abild-Pedersen, J. K. Nørskov, *Nature* **2004**, *427*, 426.
[23] J. A. Farmer, C. T. Campbell, *Science* **2010**, *329*, 933.
[24] H. Han, J. Park, S. Y. Nam, K. J. Kim, G. M. Choi, S. S. P. Parkin, H. M. Jang, J. T. S. Irvine, *Nat. Commun.* **2019**, *10*, 1471.
[25] D. Neagu, V. Kyriakou, I.-L. Roiban, M. Aouine, C. Tang, A. Caravaca, K. Kousi, I. Schreur-Piet, I. S. Metcalfe, P. Vernoux, M. C. M. Van De Sanden, M. N. Tsampas, *ACS Nano* **2019**, *13*, 12996.
[26] I. Hamada, A. Uozumi, Y. Morikawa, A. Yanase, H. Katayama-Yoshida, *J. Am. Chem. Soc.* **2011**, *133*, 18506.
[27] Y. Nishihata, J. Mizuki, T. Akao, H. Tanaka, M. Uenishi, M. Kimura, T. Okamoto, N. Hamada, *Nature* **2002**, *418*, 164.
[28] J.-H. Myung, D. Neagu, D. N. Miller, J. T. S. Irvine, *Nature* **2016**, *537*, 528.
[29] V. Kyriakou, R. K. Sharma, D. Neagu, F. Peeters, O. De Luca, P. Rudolf, A. Pandiyan, W. Yu, S. W. Cha, S. Welzel, M. C. M. Sanden, M. N. Tsampas, *Small Methods* **2021**, *5*, 2100868.
[30] J. Suriyaprakash, Y. B. Xu, Y. L. Zhu, L. X. Yang, Y. L. Tang, Y. J. Wang, S. Li, X. L. Ma, *Sci. Rep.* **2017**, *7*, 8343.
[31] V. Kyriakou, D. Neagu, E. I. Papaioannou, I. S. Metcalfe, M. C. M. Van De Sanden, M. N. Tsampas, *Appl. Catal., B* **2019**, *258*, 117950.
[32] Y.-R. Jo, B. Koo, M.-J. Seo, J. K. Kim, S. Lee, K. Kim, J. W. Han, W. Jung, B.-J. Kim, *J. Am. Chem. Soc.* **2019**, *141*, 6690.
[33] M. Chanthanumataporn, J. Hui, X. Yue, K. Kakinuma, J. T. S. Irvine, K. Hanamura, *Electrochim. Acta* **2019**, *306*, 159.
[34] L. Bai, H. Li, Z. Yan, X. Hao, M. Ke, K. Xie, B. Li, *Adv. Mater. Interfaces* **2021**, *8*, 2001598.
[35] Z. Sun, W. Fan, Y. Bai, *Adv. Sci.* **2022**, *9*, 2200250.
[36] W. Fan, B. Wang, R. Gao, G. Dimitrakopoulos, J. Wang, X. Xiao, L. Ma, K. Wu, B. Yildiz, J. Li, *J. Am. Chem. Soc.* **2022**, *144*, 7657.
[37] J. Faye, A. Baylet, M. Trentesaux, S. Royer, F. Dumeignil, D. Duprez, S. Valange, J.-M. Tatibouët, *Appl. Catal., B* **2012**, *126*, 134.
[38] Q. Ji, L. Bi, J. Zhang, H. Cao, X. S. Zhao, *Energy Environ. Sci.* **2020**, *13*, 1408.
[39] Y. Zhu, X. Zhong, S. Jin, H. Chen, Z. He, Q. Liu, Y. Chen, *J. Mater. Chem. A* **2020**, *8*, 10957.
[40] Q. Kang, J. Cao, Y. Zhang, L. Liu, H. Xu, J. Ye, *J. Mater. Chem. A* **2013**, *1*, 5766.
[41] L. Ye, C. Pan, M. Zhang, C. Li, F. Chen, L. Gan, K. Xie, *ACS Appl. Mater. Interfaces* **2017**, *9*, 25350.
[42] J. Zhang, K. Xie, Y. Gan, G. Wu, B. Ding, Y. Zhang, Y. Wu, *New J. Chem.* **2014**, *38*, 3434.
[43] Y. Gao, D. Chen, M. Saccoccio, Z. Lu, F. Ciucci, *Nano Energy* **2016**, *27*, 499.
[44] M. A. Lieberman, A. J. Lichtenberg, *Principles of Plasma Discharges and Materials Processing: Second Edition*, Wiley, Germany **2005**, p. 1, https://doi.org/10.1002/0471724254.
[45] B. Bharti, S. Kumar, H. N. Lee, R. Kumar, *Sci. Rep.* **2016**, *6*, 1.
[46] Y. Lu, A. Ma, Y. Yu, R. Tan, C. Liu, P. Zhang, D. Liu, J. Gui, *ACS Sustainable Chem. Eng.* **2019**, *7*, 2906.
[47] L. Xu, Q. Jiang, Z. Xiao, X. Li, J. Huo, S. Wang, L. Dai, *Angew. Chem., Int. Ed.* **2016**, *55*, 5277.
[48] Y. Gao, Z. Lu, T. L. You, J. Wang, L. Xie, J. He, F. Ciucci, *J. Phys. Chem. Lett.* **2018**, *9*, 3772.
[49] Z. O. Shi, C. Chern, S. Liang, Y. Lu, A. Satari, *MRS Online Proc. Libr.* **2011**, *335*, 107.
[50] W. D. Luedtke, U. Landman, *Phys. Rev. B* **1991**, *44*, 5970.
[51] I. Levchenko, K. Ostrikov, D. Mariotti, *Carbon* **2009**, *47*, 344.
[52] I. Levchenko, K. Ostrikov, K. Diwan, K. Winkler, D. Mariotti, *Appl. Phys. Lett.* **2008**, *93*, 183102.
[53] I. Levchenko, K. Ostrikov, D. Mariotti, V. Švrček, *Carbon* **2009**, *47*, 2379.
[54] R. L. Heinisch, F. X. Bronold, H. Fehske, *Phys. Rev. B: Condens. Matter Mater. Phys.* **2012**, *85*, 075323.
[55] E. I. Papaioannou, D. Neagu, W. K. W. Ramli, J. T. S. Irvine, I. S. Metcalfe, *Top. Catal.* **2019**, *62*, 1149.
[56] R. J. Gorte, J. M. Vohs, *Curr. Opin. Colloid Interface Sci.* **2009**, *14*, 236.
[57] W. T. Wallace, B. K. Min, D. W. Goodman, *Top. Catal.* **2005**, *34*, 17.
[58] G. Kresse, J. Furthmüller, *Comput. Mater. Sci.* **1996**, *6*, 15.
[59] G. Kresse, J. Hafner, *Phys. Rev. B* **1994**, *49*, 14251.
[60] G. Kresse, J. Furthmüller, *Phys. Rev. B* **1996**, *54*, 11169.
[61] G. Kresse, J. Hafner, *Phys. Rev. B* **1993**, *47*, 558.
[62] P. E. Blöchl, *Phys. Rev. B* **1994**, *50*, 17953.
[63] G. Kresse, D. Joubert, *Phys. Rev. B* **1999**, *59*, 1758.
[64] J. D. Gale, A. L. Rohl, *Mol. Simul.* **2011**, *29*, 291.
[65] N. D. Wood, D. M. Teter, J. S. Tse, R. A. Jackson, D. J. Cooke, L. J. Gillie, S. C. Parker, M. Molinari, *J. Solid State Chem.* **2021**, *303*, 122523.